

FOURIER ANALYSIS OF BLAZAR VARIABILITY: KLEIN-NISHINA EFFECTS AND THE JET SCATTERING ENVIRONMENT

JUSTIN D. FINKE

U.S. Naval Research Laboratory, Code 7653, 4555 Overlook Ave. SW, Washington, DC, 20375-5352

PETER A. BECKER

School of Physics, Astronomy, and Computational Sciences, MS 5C3, George Mason University, 4400 University Drive, Fairfax, VA 22030

accepted by ApJ; June 28, 2021

ABSTRACT

The strong variability of blazars can be characterized by power spectral densities (PSDs) and Fourier frequency-dependent time lags. In previous work, we created a new theoretical formalism for describing the PSDs and time lags produced via a combination of stochastic particle injection and emission via the synchrotron, synchrotron self-Compton, and external Compton (EC) processes. This formalism used the Thomson cross section and simple δ -function approximations to model the synchrotron and Compton emissivities. Here we expand upon this work, using the full Compton cross section and detailed and accurate emissivities. Our results indicate good agreement between the PSDs computed using the δ -function approximations and those computed using the accurate expressions, provided the observed photons are produced primarily by electrons with energies exceeding the lower limit of the injected particle population. Breaks are found in the PSDs at frequencies corresponding to the cooling timescales of the electrons primarily responsible for the observed emission, and the associated time lags are related to the difference in electron cooling timescales between the two energy channels, as expected. If the electron cooling timescales can be determined from the observed time lags and/or the observed EC PSDs, then one could in principle use the method developed here to determine the energy of the external seed photon source for EC, which is an important unsolved problem in blazar physics.

Subject headings: BL Lacertae objects: general — quasars: general — radiation mechanisms: non-thermal — galaxies: active — galaxies: jets

1. INTRODUCTION

Blazars, active galactic nuclei (AGN) with jets aligned with our line of sight, relativistically beam nonthermal radiation towards the Earth. This emission extends across the electromagnetic spectrum, from radio to γ rays. Although the observed radio emission probably comes from the superposition of many self-absorbed synchrotron components spread out over several parsecs (Konigl 1981), the location along the jet where the higher-frequency emission originates is a matter of some controversy. This is particularly true for the most powerful class of blazars, the flat spectrum radio quasars (FSRQs) with strong broad emission lines. These objects are thought to emit γ -rays primarily through Compton scattering of an external radiation field (known as external Compton or EC). However, the primary external radiation field for EC is not known, and could be provided by the accretion disk (Dermer & Schlickeiser 1993, 2002), the broad line region (BLR; Sikora et al. 1994), or the dust torus (Kataoka et al. 1999; Błażejowski et al. 2000). This uncertainty in the seed photon source reflects the uncertainty in the location along the jet of the primary γ -ray emitting region, which one would expect to be within ~ 0.1 pc from the black hole (BH) if the scattering of disk radiation dominates, or between ~ 0.1 and

~ 1 pc if the scattering of BLR emission dominates, or $\gtrsim 1$ pc if the scattering of dust torus emission dominates (Ghisellini & Tavecchio 2009; Sikora et al. 2009).

The association of γ -ray flares with the ejection of superluminal components (e.g., Marscher et al. 2012) indicates that the flares are coincident with the 43 GHz core, which is likely located at \gtrsim a few pc from the black hole, outside the BLR (although see Nalewajko et al. 2014). The detection of $\gtrsim 100$ GeV γ rays from FSRQs also indicates the γ rays must originate from inside the BLR to avoid $\gamma\gamma$ absorption with BLR photons (e.g., Aleksić et al. 2011). However, rapid γ -ray variability observed in FSRQs such as 3C 454.3 (Tavecchio et al. 2010), PKS 1510–089 (Brown 2013; Saito et al. 2013) and 4C 21.35 (also known as PKS 1222+21; Aleksić et al. 2011) limits the size of the emitting region, and, assuming the emitting region takes up the entire cross section of a conical jet, implies that it should be within ~ 0.1 pc of the black hole, and hence inside the BLR. Dotson et al. (2012) point out a way to distinguish between these scenarios based on the different cooling timescales at two energies if the seed photons are from the BLR (e.g. with dimensionless energy for Ly α $\epsilon_0 = E_0/m_e c^2 = 2 \times 10^{-5}$) or from the dust torus (e.g. ~ 1000 K dust producing photons with dimensionless energy $\epsilon_0 = 5 \times 10^{-7}$) due to the variation of the Compton cross-section at high energies.

Blazars are bright and highly variable at all wave-

lengths. Their variability appears stochastic, characterized by power-law colored noise in their power spectral densities (PSDs) at all wavelengths, including radio (e.g., Trippe et al. 2011; Park & Trippe 2014), optical (e.g., Chatterjee et al. 2012; Wehrle et al. 2013; Edelson et al. 2013; Revalski et al. 2014), X-rays (e.g., Zhang et al. 1999; Kataoka et al. 2001; Zhang 2002), and γ rays (e.g., Aharonian et al. 2007; Abdo et al. 2010; Nakagawa & Mori 2013). Despite the popularity of PSDs for characterizing blazar variability, until recently a theoretical motivation has been lacking. Previously, we presented a new theoretical formalism for the modeling and interpretation of these sources (Finke & Becker 2014, hereafter Paper I). This work was based on solving the Fourier-transformed electron transport (continuity) equation for the case of synchrotron and Thomson cooling, yielding a solution for the electron distribution as a function of Fourier frequency. This solution was then combined with simple δ -function approximations for synchrotron and Compton scattering emission to predict the expected PSDs and Fourier frequency-dependent time lags one would expect to observe from blazars. We showed that these Fourier transform-related data products contain detailed information about the characteristic timescales for particle escape, energy losses, and light crossing in the emission region, which is taken to be an outflowing spherical plasma blob. Several of these features were also noted by Mastichiadis et al. (2013).

Here we extend the work presented in Paper I, by solving the electron continuity equation with the full Compton cooling rates, including Klein-Nishina effects (Section 2). We then compute the synchrotron and EC PSDs, going beyond the simple δ -function approximations adopted in Paper I and employing well-known precise expressions for the synchrotron emissivity and Compton scattering cross section (Section 3). We also improve on our previous work by incorporating the light travel time effects specific to a spherical geometry, as described by Zacharias & Schlickeiser (2013). We do this in the context of EC emission from FSRQs. In Section 4 we compute the associated time lags, and in Section 6 we describe how the electron cooling timescales, obtained from spectral breaks of PSDs, can be used to constrain the seed photon energy of the external radiation source for EC. This method is very close to the one outlined by Dotson et al. (2012), except that we suggest using PSDs to obtain the cooling timescales, rather than directly observing the decaying part of the flare light curve.

Note that this paper deals with the PSDs and time lags from nonthermal emission from relativistic jets. The PSDs from coronae in Galactic black holes and AGN exhibit breaks correlated with the mass of the black hole (McHardy et al. 2006). This is true for the emission from the coronae of AGN with jets as well (e.g., Chatterjee et al. 2009, 2011). There is some theoretical indication that coronal emission, reflected off of an accretion disk, can create Fourier frequency-dependent time lags that may be related to black hole mass (Emmanoulopoulos et al. 2014). However, in this paper, we consider only nonthermal jet emission, beamed away from the jet, so that no such features are expected. There is no expected relation between black hole mass and PSDs and time lags in our model. Although there may be a connection between jet and coronal emission,

we do not consider such an effect here.

2. ELECTRON DISTRIBUTION IN THE FOURIER FREQUENCY DOMAIN

Consider a spherical homogeneous “blob” of Thomson-thin plasma of radius R containing nonthermal electrons and positrons (both of which are hereafter referred to as electrons) at highly relativistic energies, and a tangled magnetic field of strength B . The electron distribution is assumed to be isotropic and the number of electrons between Lorentz factors γ and $\gamma + d\gamma$ as a function of time t is $N_e(\gamma; t)$. Electrons may be injected into the blob at a rate $Q(\gamma, t)$, lose or gain energy at a rate $\dot{\gamma}(\gamma, t)$, and escape from the blob on a timescale $t_{\text{esc}}(\gamma, t)$. In this case, the evolution of $N_e(\gamma; t)$ is described by (e.g., Mastichiadis & Kirk 1995; Chiaberge & Ghisellini 1999; Li & Kusunose 2000; Böttcher & Chiang 2002; Chen et al. 2011, 2012)

$$\frac{\partial N_e}{\partial t} + \frac{\partial}{\partial \gamma}[\dot{\gamma}(\gamma, t)N_e(\gamma; t)] + \frac{N_e(\gamma; t)}{t_{\text{esc}}(\gamma, t)} = Q(\gamma, t). \quad (1)$$

We will further assume that $\dot{\gamma}$, t_{esc} , and R are independent of t . In this case, taking the Fourier transform of both sides of Equation (1) gives

$$-2\pi i f \tilde{N}_e(\gamma, f) + \frac{\partial}{\partial \gamma}[\dot{\gamma}(\gamma) \tilde{N}_e(\gamma, f)] + \frac{\tilde{N}_e(\gamma, f)}{t_{\text{esc}}(\gamma)} = \tilde{Q}(\gamma, f), \quad (2)$$

where the tilde refers to the Fourier transform¹, f is the Fourier frequency, $\omega = 2\pi f$ is the angular Fourier frequency, and $\tilde{Q}(\gamma, f)$ is the Fourier transformed source term. It was shown in Paper I that if $\dot{\gamma} \leq 0$ and t_{esc} is independent of γ then the solution to Equation (2) is

$$\tilde{N}_e(\gamma, f) = \frac{1}{|\dot{\gamma}(\gamma)|} \int_{\gamma}^{\infty} d\gamma' \tilde{Q}(\gamma', f) \times \exp \left[- \left(\frac{1}{t_{\text{esc}}} - i\omega \right) \int_{\gamma}^{\gamma'} \frac{d\gamma''}{|\dot{\gamma}(\gamma'')|} \right]. \quad (3)$$

We make the *ansatz* that the Fourier-transformed source terms is

$$\tilde{Q}(\gamma, f) = Q_0 (f/f_0)^{-a/2} \gamma^{-q} H(\gamma; \gamma_1, \gamma_2) H(f; f_1, f_2) \quad (4)$$

where

$$H(x; a, b) = \begin{cases} 1 & a < x < b \\ 0 & \text{otherwise} \end{cases} \quad (5)$$

is the boxcar function. We showed in Paper I that the normalization constant

$$Q_0 = \frac{2\pi \Delta t \langle L_{\text{inj}} \rangle}{m_e c^2 G \sqrt{I_r^2 + I_i^2 - 2I_r I_0 + I_0^2}} \quad (6)$$

where G , I_r , I_i , and I_0 are integrals defined in Appendix B of Paper I, and $\langle L_{\text{inj}} \rangle$ is the root mean squared power injected in electrons over a time interval Δt , so that Δt is the duration of the light curve.

We will take into account two energy loss (i.e., cooling) processes for $\dot{\gamma}(\gamma)$: synchrotron and EC. We neglect

¹ See Paper I for the definitions of the Fourier transform and its inverse used here.

adiabatic losses, since we assume R is independent of t . The synchrotron cooling rate is given by

$$-\dot{\gamma}_{sy}(\gamma) = \frac{4c\sigma_T}{3m_e c^2} u_B \gamma^2 \quad (7)$$

where

$$u_B = \frac{B^2}{8\pi}, \quad (8)$$

is the magnetic energy density, c is the speed of light, m_e is the electron mass, and σ_T is the Thomson cross section. The Compton cooling rate, valid in the Thomson through Klein-Nishina regimes, for the case of scattering of an external, isotropic, monochromatic radiation field, is given by

$$-\dot{\gamma}_{EC}(\gamma) = \frac{3c\sigma_T u_0}{8m_e c^2 \epsilon_0^2} G_{BMS}(\gamma \epsilon_0) \quad (9)$$

where u_0 and ϵ_0 are the energy density and dimensionless photon energy, respectively, of the external radiation field measured in the frame of the host galaxy, and

$$\begin{aligned} G_{BMS}(x) = & \frac{8}{3} x \frac{1+5x}{(1+4x)^2} - \frac{4x}{1+4x} \left(\frac{2}{3} + \frac{1}{2x} + \frac{1}{8x^2} \right) \\ & + \ln(1+4x) \\ & \times \left(1 + \frac{3}{x} + \frac{3}{4} \frac{1}{x^2} + \frac{\ln[1+4x]}{2x} - \frac{\ln[4x]}{x} \right) \\ & - \frac{5}{2} \frac{1}{x} + \frac{1}{x} \sum_{n=1}^{\infty} \frac{(1+4x)^{-n}}{n^2} - \frac{\pi^2}{6x} - 2 \end{aligned} \quad (10)$$

(Böttcher, Mause, & Schlickeiser 1997). A simple and fairly accurate approximation for the Compton cooling rate is given by Moderski et al. (2005), and it is

$$-\dot{\gamma}_{EC,M}(\gamma) = \frac{4c\sigma_T}{3m_e c^2} u_0 \gamma^2 M_0(4\gamma \epsilon_0) \quad (11)$$

where

$$M_0(x) = \frac{1}{(1+x)^{3/2}}. \quad (12)$$

Naturally, the total cooling rate from synchrotron and EC losses is

$$\dot{\gamma}(\gamma) = \dot{\gamma}_{sy}(\gamma) + \dot{\gamma}_{EC}(\gamma). \quad (13)$$

We neglect the effects of SSC cooling, which can be quite complicated (Schlickeiser 2009; Schlickeiser et al. 2010; Zacharias & Schlickeiser 2010, 2012a,b, 2013; Zacharias 2014).

3. OBSERVED PSDS

Now consider the case where the plasma blob described in Section 2 is moving with small angle $\theta \ll 1$ to our line of sight at a speed that is a fraction β that of light (in the host galaxy frame) giving it a Lorentz factor $\Gamma = (1-\beta^2)^{-1/2}$ and a Doppler factor $\delta_D = [\Gamma(1-\beta \cos \theta)]^{-1}$. The plasma blob comes from a supermassive black hole in a galaxy at a cosmological distance with cosmological redshift z . Primed quantities refer to the frame comoving with the blob, while unprimed quantities refer to

the observer's frame, except for the quantities related to the external radiation field, ϵ_0 and u_0 which are in the frame of the host galaxy, so that $\epsilon'_0 = \Gamma \epsilon_0$ and $u'_0 \approx \Gamma^2 u_0$.

Below we describe the observed νF_ν flux in the time domain ($F(\epsilon, t)$) and in the Fourier frequency domain ($\tilde{F}(\epsilon, f)$) for synchrotron and EC for the simple δ -function approximations and for the more precise expressions, and compare them with each other. This uses the result for $\tilde{N}_e(\gamma, f)$ described in Section 2. The PSD can be found from the Fourier transformed flux by

$$S(\epsilon, f) = |\tilde{F}(\epsilon, f)|^2 = \tilde{F}(\epsilon, f) \tilde{F}^*(\epsilon, f) \quad (14)$$

where the asterisk denotes the complex conjugate. In Paper I, we calculated the synchrotron emission including light travel time effects in a very simple, cylindrical geometry. Here, we include light travel time effects consistent with spherical geometry, using the results of Zacharias & Schlickeiser (2013). See Appendix A for details.

3.1. Synchrotron

3.1.1. Delta Function Approximation

With the δ -function approximation, synchrotron photons with observed energy ϵ are created by electrons with a comoving Lorentz factor given by

$$\gamma'_{sy} = \sqrt{\frac{\epsilon(1+z)}{\delta_D \epsilon_B}}, \quad (15)$$

with corresponding total radiated power per electron (cf. Equation (7))

$$\dot{P}_e = -\dot{\gamma}_{sy}(\gamma) m_e c^2 = \frac{4c\sigma_T}{3} u_B \gamma^2. \quad (16)$$

The corresponding νF_ν synchrotron flux as a function of time t (including light travel time effects) if the blob has a tangled comoving magnetic field B is

$$\begin{aligned} F^{sy,\delta}(\epsilon, t) = & \frac{6K_{sy,\delta}(1+z)}{\delta_D t_{lc}} \int_0^{2R'/c} dt' \left[\frac{t'c}{2R'} - \left(\frac{t'c}{2R'} \right)^2 \right] \\ & \times N_e \left(\gamma'_{sy}; \frac{t\delta_D}{1+z} - t' \right) \end{aligned} \quad (17)$$

where N_e is the comoving electron distribution,

$$t_{lc} = \frac{2R'(1+z)}{c\delta_D} \quad (18)$$

denotes the light-crossing time for the spherical blob,

$$K_{sy,\delta} = \frac{\delta_D^4}{6\pi d_L^2} c\sigma_T u_B \gamma'^3_{sy}, \quad (19)$$

$\epsilon_B = B/B_{cr}$, and $B_{cr} = 4.414 \times 10^{13}$ G.

Similar to Paper I, the Fourier transform of this is

$$\begin{aligned} \tilde{F}^{sy,\delta}(\epsilon, f) = & \frac{6K_{sy,\delta}(1+z)}{2\pi i f t_{lc} \delta_D} \tilde{N}_e \left(\gamma'_{sy}, \frac{(1+z)f}{\delta_D} \right) \\ & \times \left\{ \exp \left[\frac{4\pi i f (1+z) R'}{c\delta_D} \right] - 1 \right\}. \end{aligned} \quad (20)$$

3.1.2. Exact Synchrotron Emissivity

The νF_ν synchrotron flux as a function of time t including light travel time effects is given by

$$F^{sy}(\epsilon, t) = \frac{6K_{sy}(1+z)}{\delta_D t_{lc}} \int_0^{2R'/c} dt' \left[\frac{t'c}{2R'} - \left(\frac{t'c}{2R'} \right)^2 \right] \times \int_1^\infty d\gamma' N'_e \left(\gamma'; \frac{t\delta_D}{1+z} - t' \right) R_{CS} \left(\frac{2\epsilon(1+z)}{3\epsilon_B \delta_D \gamma'^2} \right) \quad (21)$$

where

$$K_{sy} = \frac{\sqrt{3}\delta_D^3 \epsilon (1+z) e^3 B}{4\pi \hbar d_L^2} \quad (22)$$

and

$$R_{CS}(x) = \frac{x}{2} \int_0^\pi d\theta \sin \theta \int_{x/\sin \theta}^\infty dy K_{5/3}(y) \quad (23)$$

is the function from Crusius & Schlickeiser (1986). The corresponding comoving power is again given by Equation (16). Accurate approximations to $R_{CS}(x)$ are given by Zirakashvili & Aharonian (2007), Finke, Dermer, & Böttcher (2008), and Joshi & Böttcher (2011). Following the procedure outlined in Paper I, the Fourier transformed synchrotron flux using this precise expression is given by

$$\tilde{F}^{sy}(\epsilon, f) = \frac{6K_{sy}(1+z)}{2\pi i f t_{lc} \delta_D} \left\{ \exp \left[\frac{4\pi i f (1+z) R'}{c \delta_D} \right] - 1 \right\} \times \int_1^\infty d\gamma' \tilde{N}'_e \left(\gamma'; \frac{(1+z)f}{\delta_D} \right) R_{CS} \left(\frac{2\epsilon(1+z)}{3\epsilon_B \delta_D \gamma'^2} \right). \quad (24)$$

3.2. External Compton

3.2.1. Improved Delta Function Approximation

In Paper I we used a δ -function approximation for Compton scattering that was only valid in the Thomson regime. Here we make use of a very useful δ -approximation for Compton scattering by Moderski et al. (2005) that is fairly accurate (to within about 10%) in the Thomson ($4\delta_D \gamma'_{EC} \epsilon_0 \ll 1$) through extreme Klein-Nishina (KN; $4\delta_D \gamma'_{EC} \epsilon_0 \gg 1$) regimes. We assume the external radiation field is monochromatic with dimensionless energy ϵ_0 that is isotropic in the frame of the host galaxy. Including light travel time effects, this yields for the EC flux as a function of time

$$F^{EC,\delta}(\epsilon, t) = \frac{6K_{EC,\delta}(1+z)}{\delta_D t_{lc}} \times M_0(4\delta_D \gamma'_{EC} \epsilon_0) M_2(4\delta_D \gamma'_{EC} \epsilon_0) \times \int_0^{2R'/c} dt' \left[\frac{t'c}{2R'} - \left(\frac{t'c}{2R'} \right)^2 \right] \times N_e \left(\gamma'_{EC}; \frac{t\delta_D}{1+z} - t' \right) \quad (25)$$

where

$$K_{EC,\delta} = \frac{\delta_D^6}{3\pi d_L^2} c \sigma_T u_0 \gamma'_{EC}^3, \quad (26)$$

$$M_1(x) = \langle y \rangle = \frac{\langle \epsilon \rangle}{\gamma} = \frac{\int_0^\infty dy y J_C(x, y)}{\int_0^\infty dy J_C(x, y)}, \quad (27)$$

and

$$M_2(x) = \frac{d \ln(x)}{d \ln(x M_1(x))}. \quad (28)$$

The function $M_1(x)$ is computed using the “Jones formula” Compton scattering kernel for isotropic electron and photon distributions (Jones 1968; Blumenthal & Gould 1970),

$$J_C(x, y) = 2w \ln w + (1+2w)(1-w) + \times \frac{1}{2} \frac{(xw)^2}{1+xw} (1-w), \quad (29)$$

in which

$$w = \frac{y}{x(1-y)}. \quad (30)$$

In Equation (25) one can find γ'_{EC} from ϵ by solving the equation

$$\epsilon = \frac{\delta_D \gamma'_{EC} M_1(4\delta_D \gamma'_{EC} \epsilon_0)}{1+z} \quad (31)$$

numerically for γ'_{EC} . The function $M_1(x)$ has the asymptotes

$$M_1(x) \approx \begin{cases} x/3 & x \ll 1 \text{ Thomson Regime} \\ 0.691 & x \gg 1 \text{ Extreme KN Regime} \end{cases}. \quad (32)$$

This implies

$$\gamma'_{EC} \approx \begin{cases} \frac{1}{\delta_D} \sqrt{\frac{3\epsilon(1+z)}{4\epsilon_0}} & 4\delta_D \gamma'_{EC} \epsilon_0 \ll 1 \\ \frac{\epsilon(1+z)}{(0.691)\delta_D} & 4\delta_D \gamma'_{EC} \epsilon_0 \gg 1 \end{cases} \quad (33)$$

and

$$M_2(x) \approx \begin{cases} 1/2 & x \ll 1 \text{ Thomson Regime} \\ 1 & x \gg 1 \text{ Extreme KN Regime} \end{cases}. \quad (34)$$

Fourier transformation of the approximate EC flux given by Equation (25) yields

$$\tilde{F}^{EC,\delta}(\epsilon, f) = \frac{6K_{EC,\delta}(1+z)}{2\pi i t_{lc} \delta_D} \tilde{N}_e \left(\gamma'_{EC}, \frac{(1+z)f}{\delta_D} \right) \times \left\{ \exp \left[\frac{4\pi i f (1+z) R'}{c \delta_D} \right] - 1 \right\} \times M_0(4\delta_D \gamma'_{EC} \epsilon_0) M_2(4\delta_D \gamma'_{EC} \epsilon_0). \quad (35)$$

3.2.2. Exact Compton Cross Section

We follow Dermer et al. (2009) to calculate the flux from EC emission resulting from the scattering of a monochromatic external radiation field that is isotropic in the frame of the black hole and host galaxy. We again include light travel time effects for a spherical geometry

following Zacharias & Schlickeiser (2013). This gives

$$F^{EC}(\epsilon, t) = \frac{6K_{EC}(1+z)}{\delta_D t_{lc}} \int_0^{2R'/c} dt' \left[\frac{t'c}{2R'} - \left(\frac{t'c}{2R'} \right)^2 \right] \\ \times \int_{\gamma'_{\min}}^{\gamma'_{\max}} \frac{d\gamma'}{\gamma'^2} N'_e \left(\gamma'; \frac{t\delta_D}{1+z} - t' \right) \\ \times J_C \left(4\delta_D \gamma' \epsilon_0, \frac{\epsilon(1+z)}{\gamma' \delta_D} \right) \quad (36)$$

for the νF_ν EC flux. Here

$$K_{EC} = \frac{3c\sigma_T \epsilon^2 (1+z)^2 \delta_D^2 u_0}{4\pi d_L^2 \epsilon_0^2}, \quad (37)$$

where

$$\gamma'_{\min} = \frac{\epsilon(1+z)}{2\delta_D} \left(1 + \sqrt{1 + \frac{1}{\epsilon\epsilon_0(1+z)}} \right), \quad (38)$$

and

$$\gamma'_{\max} = \gamma_2. \quad (39)$$

Recall that γ_2 denotes the high-energy cutoff in the electron injection spectrum (see Equation [4]). The Fourier-transformed EC flux is then given by

$$\tilde{F}^{EC}(\epsilon, f) = \frac{6K_{EC}(1+z)}{2\pi i f t_{lc} \delta_D} \left\{ \exp \left[\frac{4\pi i f (1+z) R'}{c \delta_D} \right] - 1 \right\} \\ \times \int_{\gamma'_{\min}}^{\gamma'_{\max}} \frac{d\gamma'}{\gamma'^2} \tilde{N}'_e \left(\gamma'; \frac{(1+z)f}{\delta_D} \right) \\ \times J_C \left(4\delta_D \gamma' \epsilon_0, \frac{\epsilon(1+z)}{\gamma' \delta_D} \right). \quad (40)$$

3.3. Numerical Results

As described in Paper I, for compact sources, the light travel time effect (Appendix A) will not be noticeable. In this section, we remove this effect to more easily display the comparison between the δ approximation and the full calculation. Without light travel time effects (valid for $R'_b \ll c\delta_D[f(1+z)]^{-1}$), the synchrotron PSDs in the δ -function approximation (Section 3.1.1) and full calculation (Section 3.1.2), respectively, can be written as

$$S^{sy,\delta}(\epsilon, f) = \left(\frac{6K_{sy,\delta}(1+z)}{\delta_D} \right)^2 \left| \tilde{N}_e \left(\gamma'_{sy}, \frac{(1+z)f}{\delta_D} \right) \right|^2, \quad (41)$$

and

$$S^{sy}(\epsilon, f) = \left(\frac{6K_{sy}(1+z)}{\delta_D} \right)^2 \\ \times \left| \int_1^\infty d\gamma' \tilde{N}'_e \left(\gamma'; \frac{(1+z)f}{\delta_D} \right) \right|^2 \\ \times R_{CS} \left(\frac{2\epsilon(1+z)}{3\epsilon_B \delta_D \gamma'^2} \right)^2. \quad (42)$$

A comparison of synchrotron PSDs computed the two different ways is shown in Figure 1. Agreement between

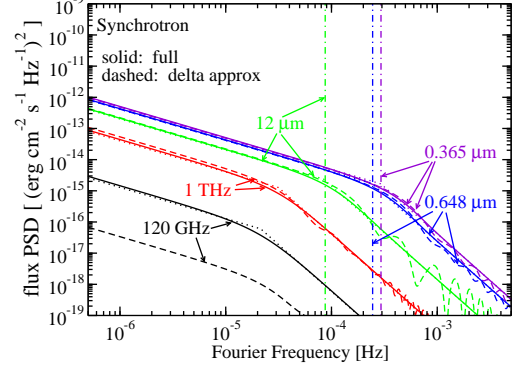


FIG. 1.— The synchrotron PSD for the δ -function approximation (dashed curves; Equation [41]), full calculation (solid curves; Equation [42]), and broken power-law fit (dotted curves; Equation [43]). Parameters are $q = 2$, $a = 1$, $t'_{\text{esc}} = 10^5$ s, $\langle L_{\text{inj}} \rangle = 10^{42}$ erg s $^{-1}$, $\Delta t = 1$ year, $\gamma_1 = 10^2$, $\gamma_2 = 10^5$, $R' = 10^{15}$ cm, $B = 1$ G, $\Gamma = \delta_D = 30$, $u_0 = 10^{-3}$ erg cm $^{-3}$, $\epsilon_0 = 5 \times 10^{-7}$, and $z = 1$. At this redshift with cosmology $(h, \Omega_m, \Omega_\Lambda) = (0.7, 0.3, 0.7)$ the luminosity distance $d_L = 2 \times 10^{28}$ cm. The observed photon frequency ($m_e c^2 \epsilon / h$) or wavelength ($hc / [m_e c^2 \epsilon]$) is shown. Dashed lines indicate $f = (3t_{\text{cool}})^{-1}$ for each curve where $t_{\text{cool}} < t_{\text{esc}}$.

the δ -function approximation and the full calculation is good, except for the 120 GHz curve. For this frequency, photons come from electrons with $\gamma' < \gamma_1$. Clearly for this range the δ -function approximation is not accurate. With an observer-frame cooling timescale defined by

$$t_{\text{cool}}(\epsilon) = \frac{1+z}{\delta_D} \int_{\gamma}^{\gamma_2} \frac{d\gamma'}{|\dot{\gamma}(\gamma')|}, \quad (43)$$

the PSDs with $t_{\text{cool}} < t_{\text{esc}}$ exhibit breaks at $f = [3t_{\text{cool}}(\epsilon)]^{-1}$. As t_{cool} gets closer and closer to t_{esc} , and eventually gets longer than t_{esc} , this approximation breaks down. For synchrotron, γ in Equation (43) is calculated from ϵ using Equation (15). The full curves “wash out” the many minima of the δ -function approximation, so that the PSDs more closely resemble broken power-laws. The break has a magnitude of 2, i.e., the break is from $S(\epsilon, f) \propto f^{-a}$ to $S(\epsilon, f) \propto f^{-(a+2)}$.

Without light travel time effects ($R'_b \ll c\delta_D[f(1+z)]^{-1}$), the EC PSDs in the δ -function approximation (Section 3.2.1) and full calculation (Section 3.2.2), respectively, can be written as

$$S^{EC,\delta}(\epsilon, f) = \left[\frac{6K_{EC,\delta}(1+z)}{\delta_D} \right. \\ \times M_0(4\delta_D \gamma'_{EC} \epsilon_0) M_2(4\delta_D \gamma'_{EC} \epsilon_0) \left. \right]^2 \\ \times \left| \tilde{N}_e \left(\gamma'_{EC}, \frac{(1+z)f}{\delta_D} \right) \right|^2, \quad (44)$$

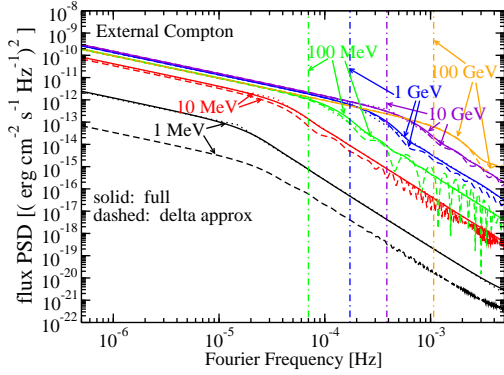


FIG. 2.— The EC PSD for the δ -function approximation (dashed curves; Equation [44]), full calculation (solid curves; Equation [45]), and broken power-law fit (dotted curves). Parameters are the same as in Figure 1. The observed photon energy ($m_e c^2 \epsilon$) is shown. Dashed-dotted lines indicate $f = (3t_{\text{cool}})^{-1}$ for each curve where $t_{\text{cool}} < t_{\text{esc}}$.

and

$$S^{EC}(\epsilon, f) = \left(\frac{6K_{EC}(1+z)}{\delta_D} \right)^2 \times \left| \int_{\gamma'_{\min}}^{\gamma'_{\max}} \frac{d\gamma'}{\gamma'^2} \tilde{N}'_e \left(\gamma'; \frac{(1+z)f}{\delta_D} \right) \right| \times J_C \left(4\delta_D \gamma' \epsilon_0, \frac{\epsilon(1+z)}{\gamma' \delta_D} \right) \Big|^2. \quad (45)$$

Figure 2 plots the EC PSDs computed the two different ways. Here for EC, γ in Equation (43) is found from ϵ by solving Equation (31) numerically. Minima features in the δ -function approximation are again washed out in the full calculation, and agreement is good, except for the 1 MeV curve, where photons are generated primarily from electrons with $\gamma' < \gamma_1$. As with the synchrotron PSDs, in the EC PSDs for $t_{\text{cool}} < t_{\text{esc}}$, breaks are seen at $f = [3t_{\text{cool}}]^{-1}$, and again this approximation is less valid as t_{cool} approaches t_{esc} .

4. TIME LAGS

Time lags as a function of Fourier frequency are given by

$$\Delta T(\epsilon_a, \epsilon_b, f) = \frac{1}{2\pi f} \arctan \left[\frac{Y_I(\epsilon_a, \epsilon_b, f)}{Y_R(\epsilon_a, \epsilon_b, f)} \right] \quad (46)$$

(e.g., Paper I) where $Y_R(\epsilon_a, \epsilon_b, f)$ and $Y_I(\epsilon_a, \epsilon_b, f)$ are defined by

$$\tilde{F}(\epsilon_a, f) \tilde{F}^*(\epsilon_b, f) = Y_R(\epsilon_a, \epsilon_b, f) + i Y_I(\epsilon_a, \epsilon_b, f). \quad (47)$$

Equations (46) and (47) above are combined with Equations (35) and (40) to compute the time lags with the Moderski approximation and full calculation for the EC time lags. The results are shown in Figure 3. Note that light travel time effects will play no part in time lags, since they are energy-independent. Our numerical results indicates that the time lags in the limits $f \ll [2\pi t_{\text{cool}}(\epsilon_b)]^{-1}$ and $f \ll [2\pi t_{\text{cool}}(\epsilon_a)]^{-1}$, are

$$\Delta T(\epsilon_a, \epsilon_b, f) \approx [t_{\text{cool}}(\epsilon_b) - t_{\text{cool}}(\epsilon_a)]/3 \quad (48)$$

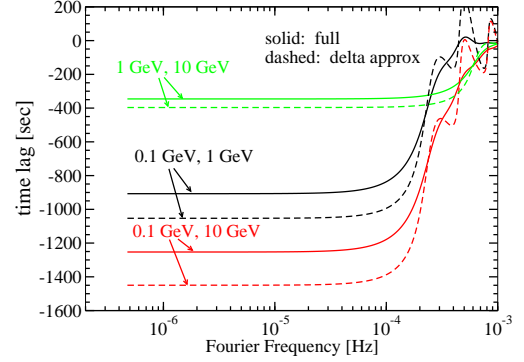


FIG. 3.— EC flux time lags. Solid curves show the lags computed with the full calculation (Equation [40]), dashed curves show the lags computed with the δ -function approximation (Equation [35]).

for the full calculation, where $t_{\text{cool}}(\epsilon)$ is the new definition from this paper, Equation (43). The Moderski δ function approximation however is about 15% higher in all cases. This is also true for synchrotron time lags, which are not shown. Clearly the δ function approximations are not as accurate for time lags as they are for PSDs.

In this paper, we use the standard convention that $\epsilon_b < \epsilon_a$ (e.g., Kroon & Becker 2014), so that positive lags refer to hard lags (i.e., the hard channel lags behind the soft channel), and negative lags to soft lags (i.e., the soft channel lags behind the hard channel). Thus, Figure 3 shows our model only reproduces soft lags. Note that this is in contrast to Paper I, where we did not use this convention. In X-ray observations of BL Lac objects, both soft lags (e.g. Zhang et al. 2002) and hard lags (e.g., Zhang 2002) have been observed. Our model can reproduce the soft lags but not the hard lags, contrary to our discussion in Section 6.2 of Paper I. This is because the continuity equation treated here only includes losses (due to synchrotron and EC emission) and does not include any energization processes. Inclusion of acceleration effects in our model may be able to explain the hard lags if the acceleration timescale is shorter than the cooling timescale, as suggested by Zhang (2002). We will explore this possibility in future work (Lewis, Becker, & Finke 2015, in preparation).

5. COMPARISON WITH OBSERVATIONS

In Section 6 of Paper I, we compared our model with several PSD observations. In this section, we update some of our conclusions, based on the improvements to our model. Results from Paper I not described below are unchanged.

5.1. Oscillatory Features

The use of the accurate expressions eliminate the oscillatory structures in the PSDs seen with the δ -approximations, so that the PSDs more closely resemble broken power-laws. Possible minima from observed PSD, such as the VHE PSD of PKS 2155–304 presented by Aharonian et al. (2007), or the QPOs observed by e.g. Lachowicz et al. (2009), Gupta et al. (2009) or Rani et al. (2010), we now believe are unlikely to be associated with the minima features predicted in Paper I. These features seem to be an artifact of the δ -function approximation and they are not present in more accurate calculations.

5.2. The γ -ray PSD of 3C 454.3

As reported by Nakagawa & Mori (2013), the LAT γ -ray PSD of 3C 454.3 has a break at a frequency of 1.5×10^{-5} Hz (although see Sobolewska et al. 2014). If at LAT energies $t_{\text{cool}} < t_{\text{esc}}$, this implies a cooling timescale of 2.3×10^5 s in the observer frame. For parameters $\Gamma = \delta_D = 30$, $B = 1.0$ G, $u_0 = 10^{-4}$ erg cm $^{-3}$, $\gamma_2 = 10^5$, and assuming the LAT is dominated by photons at 100 MeV, one can numerically solve for the seed photon energy, and obtain $\epsilon_0 = 1.8 \times 10^{-5}$, which is quite close to the value for Ly α (2.0×10^{-5} in $m_e c^2$ units). For the same set of parameters, except $u_0 = 10^{-2}$ erg cm $^{-3}$, one gets $\epsilon_0 = 7.0 \times 10^{-4}$ (or 0.36 keV), and for $u_0 = 10^{-1}$ erg cm $^{-3}$, one gets $\epsilon_0 = 3.3 \times 10^{-3}$ (or 1.7 keV). The latter two are unrealistically high for seed photon energies, and Ly α does make more sense as a seed photon source, since it is the most prominent line seen in optical spectra (e.g., Telfer et al. 2002), however this is an unrealistically low energy density. In this regard, the Klein-Nishina effects do not alter our conclusions from Paper I.

5.3. The Optical PSDs of blazars

Edelson et al. (2013) have used *Kepler* observations to identify a “bend” in the PSD of the BL Lac W2R1926+42 corresponding to a period of 4 hours. Assuming the emission detected by *Kepler* is dominated by detections at 5000 Å, and for similar parameters as in Section 5.2, with $u_0 = 10^{-4}$ erg cm $^{-3}$ one gets $\epsilon_0 = 2.3 \times 10^{-7}$, about what one would expect for scattering of dust torus emission; for $u_0 = 10^{-2}$ erg cm $^{-3}$ one gets $\epsilon_0 = 2.5 \times 10^{-5}$, about what one expects for scattering Ly α photons; and for $u_0 = 10^{-1}$ erg cm $^{-3}$ one gets $\epsilon_0 = 1.2 \times 10^{-4}$. The latter is probably an unrealistic value for ϵ_0 , and the values of u_0 for the former are about what one would expect for these seed photon sources, although for Ly α the energy density is a bit low. Thus for this source, scattering of dust torus emission seems the most likely, although this conclusion is strongly dependent on the assumed parameters. In Section 6 we describe a method of determining the seed photon source that is more model-independent.

6. METHOD FOR DETERMINING SEED PHOTON ENERGY

Here we outline a technique for determining the energy of the seed photon source for EC. We assume the external seed photon source can be approximated as isotropic in the galaxy’s frame, and that it is monochromatic with dimensionless energy ϵ_0 . We also assume from the breaks or time lags in the PSDs of blazars at several energy ranges in EC one can obtain the cooling timescale, as described in Sections 3 and 4. For example, one might find breaks in *Fermi*-LAT PSDs at $m_e c^2 \epsilon_a = 0.1$ GeV, $m_e c^2 \epsilon_b = 1.0$ GeV, and $m_e c^2 \epsilon_c = 10.0$ GeV, and thus the cooling timescales at these energies.

If one is observing synchrotron or EC, one can use Equation (43) to compute the observer frame cooling timescale from synchro-Compton losses, which we rewrite as

$$t_{\text{cool}}(\epsilon) = \frac{3(1+z)m_e c^2 \epsilon_0}{c \sigma_T u_B} \int_{x_1}^{x_2} \frac{dx}{x^2} \frac{1}{1 + A_C M_0(x)} \quad (49)$$

where

$$x_2 = 4\Gamma\gamma_2\epsilon_0 \quad (50)$$

and

$$A_C = \frac{\Gamma^2 u_0}{u_B} \quad (51)$$

is the Compton dominance, assuming $\delta_D = \Gamma$. If the cooling timescale is estimated from a PSD or time lag that is emitting synchrotron, the integral’s lower limit is

$$x_{1, sy} = 4\epsilon_0 \left(\frac{\epsilon(1+z)\delta_D}{\epsilon_B} \right)^{1/2}. \quad (52)$$

If the cooling timescale is estimated from EC, then the integral’s lower limit is

$$x_{1, EC} = 4\Gamma\gamma'_{EC}\epsilon_0 = \frac{4\epsilon\epsilon_0(1+z)}{M_1(x_{1, EC})} \approx \begin{cases} 2\sqrt{3\epsilon\epsilon_0(1+z)} & 4\Gamma\gamma'_{EC}\epsilon_0 \ll 1 \\ 4\epsilon\epsilon_0(1+z)/(0.691) & 4\Gamma\gamma'_{EC}\epsilon_0 \gg 1 \end{cases} \quad (53)$$

For computing x_1 above we have made use of the δ function approximations for synchrotron and EC, as described in Section 3.1.1 and 3.2.1. For EC, a function created from three cooling timescales,

$$r(\epsilon_a, \epsilon_b, \epsilon_c) = \frac{t_{\text{cool}}(\epsilon_a) - t_{\text{cool}}(\epsilon_c)}{t_{\text{cool}}(\epsilon_a) - t_{\text{cool}}(\epsilon_b)} \quad (54)$$

is dependent only on ϵ_0 and A_C . In principle, A_C can be determined from the broadband spectral energy distribution (e.g., Meyer et al. 2012; Finke 2013). For synchrotron, this function is additionally dependent on the ratio δ_D/ϵ_B . Observations of FSRQ synchrotron PSDs and lags will also suffer from contamination by thermal emission, from the accretion disk and dust torus. Therefore we will only be concerned with the γ -ray emission from EC.

We plot the $r(0.1 \text{ GeV}, 1.0 \text{ GeV}, 10.0 \text{ GeV})$ for different values of A_C in Figure 4. These plots demonstrate that given A_C and t_{cool} for three energies, one can estimate the energy of the seed photon source, ϵ_0 . For low values of ϵ_0 ($\epsilon_0 \lesssim 10^{-6}$), the scattering at all three energies will be in the Thomson regime, and the value will be mostly independent of ϵ_0 or A_C . Only at higher values of ϵ_0 will Klein-Nishina effects become apparent.

Although in principle it may be possible to determine ϵ_0 from PSDs or time lags computed from *Fermi*-LAT light curves, in practice this will be extremely difficult. During the brightest flares, it is possible to probe timescales ~ 1 hour (e.g., Tavecchio et al. 2010; Abdo et al. 2011; Brown 2013; Saito et al. 2013; Nalewajko 2013), but this is rare. More typically, integrations over a few days to a week are needed to significantly detect a source with the LAT (e.g., Abdo et al. 2010), so that probing the ~ 1 hour timescales necessary to detect the breaks is unlikely in most cases. So far, three FSRQs have published spectra from imaging atmospheric Cherenkov telescopes (IACTs) (Albert et al. 2008; Aleksić et al. 2011; H.E.S.S. Collaboration et al. 2013), and one more has been detected by IACTs (Mirzoyan 2015; Mukherjee 2015). It is certainly reasonable to expect that the proposed Cherenkov Telescope Array (CTA; Actis et al. 2011) will be able to

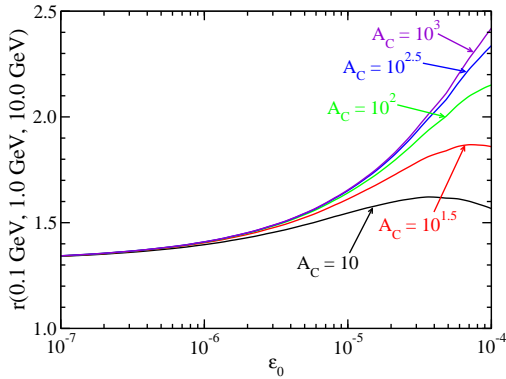


FIG. 4.— The function $r(0.1 \text{ GeV}, 1.0 \text{ GeV}, 10.0 \text{ GeV})$ from Equation (54) plotted as a function of dimensionless seed photon energy ϵ_0 for different values of Compton dominance A_C .

get significant detections with shorter integration times than the LAT, and therefore it may be able to probe these timescales. However, at higher energies, the cooling timescales will also be shorter, making the breaks more difficult to observe. If the breaks are on sub-hour timescales, a time baseline (i.e., Δt in our notation) of about 10 times the timescale of the expected break should be sufficient, so that a single night of observing would probably be a long enough baseline to observe a break. Probing short enough timescales would be a greater issue. Further, any source detected at $\gtrsim 20 \text{ GeV}$ is almost certainly making γ rays outside the BLR, otherwise the γ -rays would be attenuated by $\gamma\gamma$ absorption with the $\text{Ly}\alpha$ photons (e.g., Stern & Poutanen 2014). However, an analysis with CTA could verify our results.

The technique outlined here is similar to obtaining the cooling timescales by modeling the decay times of individual flares, as discussed by Dotson et al. (2012), although our model has a few advantages. For example, with the new method, one is able to take advantage of a long series of data, rather than individual flares, possibly leading to more statistically significant results. When modeling individual flares, it is not clear if the decrease in flux from a flare is due to radiative cooling or due to the rapid decrease in the electron acceleration rate. The disadvantage of our technique is it may be that different flares from the same object have different origins. Perhaps some flares occur close to the BH, so that the

seed photon source is from the BLR, while others occur farther away, so that the seed photon source is the dust torus. PSDs based on long timescale light curves would have a difficult time disentangling these cases.

7. DISCUSSION

We have expanded upon our previous theoretical scenario for computing PSDs and time lags (Paper I). We have included the full Compton cross section in our solution to the Fourier-transformed continuity equation. As in Paper I, we find breaks in the resulting PSDs associated with the cooling timescale, however, we must revise our definition of the cooling timescale. We have compared the simple δ -function approximations for synchrotron and Compton emission to more accurate expressions. For PSDs the agreement between the approximations and the accurate expressions is very good, except for photons produced primarily by electrons with $\gamma' < \gamma'_1$. As in Paper I, we find that the breaks in synchrotron and EC PSDs always have magnitudes of 2, i.e., the break is from $S(\epsilon, f) \propto f^{-a}$ to $S(\epsilon, f) \propto f^{-(a+2)}$.

At low Fourier frequencies, time lags calculated with the δ -approximations give lags about 15% greater than lags computed with the accurate expressions. The cause of the deviation is not clear. However, as in Paper I, we confirm that the time lags at low Fourier frequencies can be associated with the difference in cooling timescales of the two energy channels.

Based on our theoretical work, it seems that one could in principle measure the cooling timescale based on observations of blazar PSDs or time lags. If one can measure the cooling timescale from γ -rays produced by EC at three different energies, while also determining the Compton dominance from the blazar's broadband SED, then in principle determine the energy of the seed photon source. This would give a strong indication as to the location of the γ -ray emitting region, something which has so far eluded understanding. Such a feat is unlikely to be possible with currently operating γ -ray telescopes such as the *Fermi*-LAT, but may be possible with CTA.

We are grateful to the referee for helpful comments that have improved this manuscript, and to C. Dermer and S. Larsson for useful discussions. JDF is supported by the Chief of Naval Research.

APPENDIX

A. LIGHT TRAVEL TIME DELAY

In this section we derive the light travel time effect, directly following Zacharias & Schlickeiser (2013, c.f. Appendix C of Paper I). The spherical emitting region with radius R , volume $V = 4\pi R^3/3$ is homogeneous, with variations taking place throughout the sphere simultaneously. Its total emitting flux is F at time t , but the observer will see light from the closer part of the sphere arrive before the light from the farther part of the sphere. For the calculation of this effect, the emitting region is divided into an infinite number of “slices” each with infinitesimally small thickness dx emitting flux dF at time t . The slices are cut perpendicular to the direction of the observer so that each one has radius

$$y = \sqrt{R^2 - (R - x)^2}, \quad (\text{A1})$$

cross sectional area

$$A = \pi y^2 = \pi(2Rx - x^2), \quad (\text{A2})$$

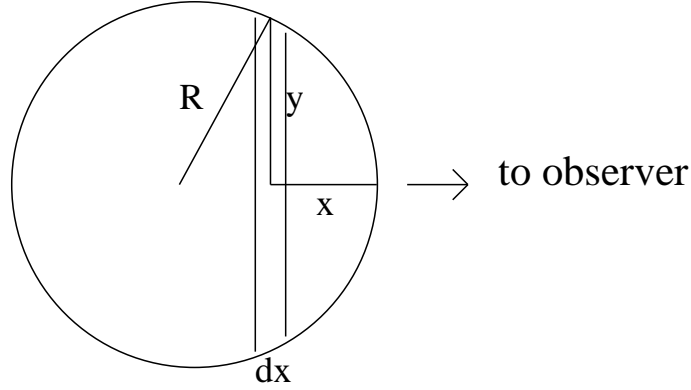


FIG. 5.— Geometric sketch of spherical emitting blob for the purpose of computing light travel time effects. This sketch is in the frame co-moving with the blob.

and volume

$$dV = A dx \quad (\text{A3})$$

(see Figure 5). The flux emitted by each slice as a fraction of the whole is proportional to the volume of the slice as a fraction of the whole, i.e.,

$$\frac{dF}{F} = \frac{dV}{V} . \quad (\text{A4})$$

The observer sees flux from each slice delayed by time $t = x/c$ so that the observed flux at time t_{obs} is

$$\begin{aligned} F_{obs}(t_{obs}) &= \int dF(t_{obs} - t) = \int F(t_{obs} - t) \frac{dV(t_{obs})}{V} . \\ &= \frac{3c}{R} \int_0^{2R/c} dt F(t_{obs} - t) \left[\frac{tc}{2R} - \left(\frac{tc}{2R} \right)^2 \right] . \end{aligned} \quad (\text{A5})$$

Combining this with standard formulae for synchrotron and Compton emission for $F(t)$ (e.g., Dermer & Menon 2009) leads to the results in Sections 3.1 and 3.2.

REFERENCES

- Abdo, A. A., et al. 2010, *ApJ*, 722, 520
—, 2011, *ApJ*, 733, L26
Actis, M., et al. 2011, *Experimental Astronomy*, 32, 193
Aharonian, F., et al. 2007, *ApJ*, 664, L71
Albert, J., et al. 2008, *Science*, 320, 1752
Aleksić, J., et al. 2011, *ApJ*, 730, L8
Błażejowski, M., Sikora, M., Moderski, R., & Madejski, G. M. 2000, *ApJ*, 545, 107
Blumenthal, G. R., & Gould, R. J. 1970, *Reviews of Modern Physics*, 42, 237
Böttcher, M., & Chiang, J. 2002, *ApJ*, 581, 127
Böttcher, M., Mause, H., & Schlickeiser, R. 1997, *A&A*, 324, 395
Brown, A. M. 2013, *MNRAS*, 431, 824
Chatterjee, R., et al. 2009, *ApJ*, 704, 1689
—, 2011, *ApJ*, 734, 43
—, 2012, *ApJ*, 749, 191
Chen, X., Fossati, G., Böttcher, M., & Liang, E. 2012, *MNRAS*, 424, 789
Chen, X., Fossati, G., Liang, E. P., & Böttcher, M. 2011, *MNRAS*, 416, 2368
Chiaberge, M., & Ghisellini, G. 1999, *MNRAS*, 306, 551
Crusius, A., & Schlickeiser, R. 1986, *A&A*, 164, L16
Dermer, C. D., Finke, J. D., Krug, H., & Böttcher, M. 2009, *ApJ*, 692, 32
Dermer, C. D., & Menon, G. 2009, *High Energy Radiation from Black Holes: Gamma Rays, Cosmic Rays, and Neutrinos*
Dermer, C. D., & Schlickeiser, R. 1993, *ApJ*, 416, 458
—, 2002, *ApJ*, 575, 667
Dotson, A., Georganopoulos, M., Kazanas, D., & Perlman, E. S. 2012, *ApJ*, 758, L15
Edelson, R., Mushotzky, R., Vaughan, S., Scargle, J., Gandhi, P., Malkan, M., & Baumgartner, W. 2013, *ApJ*, 766, 16
Emmanoulopoulos, D., Papadakis, I. E., Dovčiak, M., & McHardy, I. M. 2014, *MNRAS*, 439, 3931
Finke, J. D. 2013, *ApJ*, 763, 134
Finke, J. D., & Becker, P. A. 2014, *ApJ*, 791, 21
Finke, J. D., Dermer, C. D., & Böttcher, M. 2008, *ApJ*, 686, 181
Ghisellini, G., & Tavecchio, F. 2009, *MNRAS*, 397, 985
Gupta, A. C., Srivastava, A. K., & Wiita, P. J. 2009, *ApJ*, 690, 216
H.E.S.S. Collaboration et al. 2013, *A&A*, 554, A107
Jones, F. C. 1968, *Physical Review*, 167, 1159
Joshi, M., & Böttcher, M. 2011, *ApJ*, 727, 21
Kataoka, J., et al. 1999, *ApJ*, 514, 138
—, 2001, *ApJ*, 560, 659
Konigl, A. 1981, *ApJ*, 243, 700
Kroon, J. J., & Becker, P. A. 2014, *ApJ*, 785, L34
Lachowicz, P., Gupta, A. C., Gaur, H., & Wiita, P. J. 2009, *A&A*, 506, L17
Li, H., & Kusunose, M. 2000, *ApJ*, 536, 729
Marscher, A. P., Jorstad, S. G., Agudo, I., MacDonald, N. R., & Scott, T. L. 2012, *arXiv:1204.6707*
Mastichiadis, A., & Kirk, J. G. 1995, *A&A*, 295, 613
Mastichiadis, A., Petropoulou, M., & Dimitrakoudis, S. 2013, *MNRAS*, 434, 2684
McHardy, I. M., Koerding, E., Knigge, C., Uttley, P., & Fender, R. P. 2006, *Nature*, 444, 730
Meyer, E. T., Fossati, G., Georganopoulos, M., & Lister, M. L. 2012, *ApJ*, 752, L4
Mirzoyan, R. 2015, *The Astronomer's Telegram*, 7080, 1

- Moderski, R., Sikora, M., Coppi, P. S., & Aharonian, F. 2005, MNRAS, 363, 954
- Mukherjee, R. 2015, The Astronomer's Telegram, 7433, 1
- Nakagawa, K., & Mori, M. 2013, ApJ, 773, 177
- Nalewajko, K. 2013, MNRAS, 430, 1324
- Nalewajko, K., Begelman, M. C., & Sikora, M. 2014, ApJ, 789, 161
- Park, J.-H., & Trippe, S. 2014, ApJ, 785, 76
- Rani, B., Gupta, A. C., Joshi, U. C., Ganesh, S., & Wiita, P. J. 2010, ApJ, 719, L153
- Revalski, M., Nowak, D., Wiita, P. J., Wehrle, A. E., & Unwin, S. C. 2014, ApJ, 785, 60
- Saito, S., Stawarz, L., Tanaka, Y. T., Takahashi, T., Madejski, G., & D'Ammando, F. 2013, ApJ, 766, L11
- Schlickeiser, R. 2009, MNRAS, 398, 1483
- Schlickeiser, R., Böttcher, M., & Menzler, U. 2010, A&A, 519, A9+
- Sikora, M., Begelman, M. C., & Rees, M. J. 1994, ApJ, 421, 153
- Sikora, M., Stawarz, L., Moderski, R., Nalewajko, K., & Madejski, G. M. 2009, ApJ, 704, 38
- Sobolewska, M. A., Siemiginowska, A., Kelly, B. C., & Nalewajko, K. 2014, ApJ, 786, 143
- Stern, B. E., & Poutanen, J. 2014, ApJ, 794, 8
- Tavecchio, F., Ghisellini, G., Bonnoli, G., & Ghirlanda, G. 2010, MNRAS, 405, L94
- Telfer, R. C., Zheng, W., Kriss, G. A., & Davidsen, A. F. 2002, ApJ, 565, 773
- Trippe, S., et al. 2011, A&A, 533, A97
- Wehrle, A. E., Wiita, P. J., Unwin, S. C., Di Lorenzo, P., Revalski, M., Silano, D., & Sprague, D. 2013, ApJ, 773, 89
- Zacharias, M. 2014, MNRAS, 443, 3001
- Zacharias, M., & Schlickeiser, R. 2010, A&A, 524, A31+
- . 2012a, MNRAS, 420, 84
- . 2012b, ApJ, 761, 110
- . 2013, ApJ, 777, 109
- Zhang, Y. H. 2002, MNRAS, 337, 609
- Zhang, Y. H., et al. 1999, ApJ, 527, 719
- . 2002, ApJ, 572, 762
- Zirakashvili, V. N., & Aharonian, F. 2007, A&A, 465, 695